Measurement of Absolute Carbon Ion Density Profile Based on CXRS Diagnostic on HL-2A Tokamak*)

Liang LIU, Deliang YU, Xiaoxue HE, Yanling WEI, Dong LI, Qian MA[1)], Wenjin CHEN, Xiaofei HE, Neng ZHANG, Zengchen YANG, Yonggao LI, Longwen YAN, Zhongbing SHI, Yi LIU and Qingwei YANG

Southwestern Institute of Physics, Chengdu 610041, China
[1)]*Baoji University of Arts and Sciences, Baoji 721000, China*

(Received 27 November 2019 / Accepted 12 June 2020)

The profile of absolute carbon ion density is calculated based on the charge exchange recombination spectroscopy (CXRS) diagnostic on HL-2A tokamak. The carbon ion concentration is derived by a combination of absolutely calibrated active spectrum intensity, neutral beam densities and effective charge exchange emission rates. The neutral beam densities for the full (E_b), one-half (E_b/2) and one-third (E_b/3) fractional beam energy components are calculated with the beam attenuation process which is determined by the beam stopping cross-section. The beam population of H^*(n = 2) to H(1 s) is evaluated, both of which contribute to the charge exchange procedure as donors. Z_{eff} profiles measured by the local impurity concentration and visible bremsstrahlung are compared.

Keywords: carbon ion density profile, neutral beam attenuation, CXRS diagnostic

DOI: 10.1585/pfr.15.2402055

1. Introduction

Carbon and other low-Z impurities are attractive for particle transport studies in the magnetically confined fusion machines because they are fully stripped throughout most of the discharges. This greatly simplifies the atomic physics (particularly ionization and recombination) which must be considered in order to arrive at the accurate measurements of transport coefficients for these ions [1–3].

The charge exchange recombination spectroscopy (CXRS) diagnostic provides an important tool to deduce the naked impurity ion density profiles. For example, the He-ash density measurement requires 10% accuracy for ITER, and the localized CXRS system is the only candidate for such a challenge [4]. There are mainly two methods to deduce the naked impurity ion density profiles based on CXRS diagnostic. One method is to couple the active spectral line intensity with neutral beam deposition calculation [5], the other one is to combine the CXRS and beam emission spectroscopy (BES) without beam deposition calculation [6].

The dominant intrinsic light impurity in HL-2A plasma is carbon, since the covered carbon material reaches nearly 40% of the total in-vessel area [7]. In this paper, the technique for the measurement of naked carbon ion density in HL-2A plasmas based on the absolutely calibrated active CVI (n = 8 - 7, 529.1 nm) intensity is introduced. There are two features in the calculation: 1) C^{6+} profiles are deduced by a self-consistent treatment in which trial C^{6+} profile shapes are iterated until agreement between the trial and calculated densities of C^{6+}(r) are achieved. 2) The charge exchange from the n = 2 level of beam neutrals is considered, which is important for the low-energy components.

On HL-2A, the impurity densities in atomic and low-ionization states at plasma edge are mainly provided by a passive visible spectroscopic diagnostic [8], and the highly ionized impurity densities are given by the extreme ultraviolet (EUV) and vacuum ultraviolet (VUV) spectrometers [9]. The measurement of fully ionized carbon density helps establish the entire carbon density profiles in different ionization states in HL-2A plasmas, for the purpose of allowing the determination of the carbon transport coefficients across the whole plasma in our future work. The Z_{eff} profiles measured by the local impurity concentration and visible bremsstrahlung are compared in this paper.

2. Diagnostic Geometry

In this work, the profile of absolute carbon ion density is calculated based on the toroidal CXRS diagnostic in Ref. [10]. Here we describe it in brief. On HL-2A tokamak, the neutral deuterium beam, equipped with four ion sources and acting as a powerful heating beam [11], is injected in the co-current direction with an injection angle of 37°, as shown in Fig. 1. The distance from the extraction surface of ion source to plasma center (R = 1.65 m with R being the major radius) is 6.27 m. The acceleration volt-

author's e-mail: liuliang@swip.ac.cn. yangqw@swip.ac.cn
*) This article is based on the presentation at the 28th International Toki Conference on Plasma and Fusion Research (ITC28).

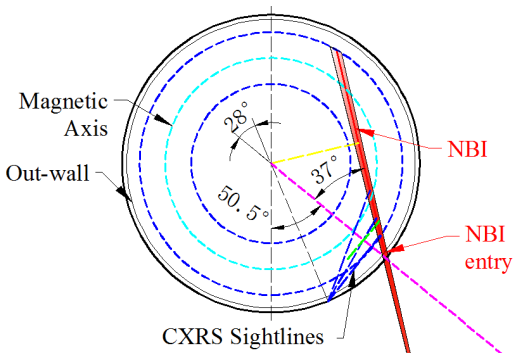

Fig. 1 Geometry of the neutral beam injection (NBI) and sight lines of CXRS diagnostic on HL-2A tokamak.

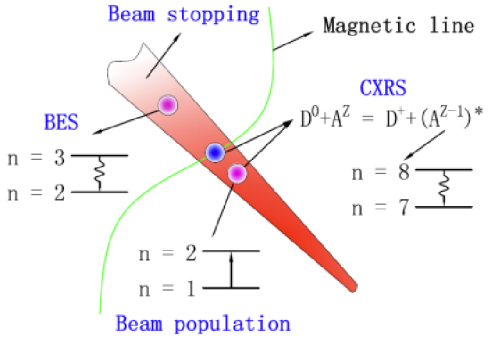

Fig. 2 Atomic processes involved in the calculation of carbon ion density.

ages of ion beams range from 20 to 54 kV. In the case of Shot 31572 for the carbon ion density calculation in this paper, the acceleration voltage is 45 kV. The neutral beam is primarily composed of three components at energies E, E/2 and E/3 arising from the extraction of D^+, D_2^+ and D_3^+ from the ion source. The collection lens focuses the visible radiation from the intersection columns of the sight lines and neutral beam onto the fiber optics. This diagnostic consists of 32 channels and the field of view (FOV) covers the region from R = 1.60 to 2.04 m (the location of magnetic axis is around R = 1.65 m) along the neutral beam trajectory, realizing a spatial resolution of ~ 1 cm. The angles between the sight lines and NBI axis range from 34.3° to 52°. With a high-spectral resolution spectrometer coupled with a back-illuminated CCD (Andor iXon Ultra 897), i.e., the reciprocal linear dispersion of 0.0117 nm/pixel at 529 nm, the time resolution of 5 ms is routinely applied with respect to the signal-to-noise ratio. The absolute intensity calibration for this diagnostic has been provided by a standard integrating sphere (Labsphere SC 6000).

3. Calculation Results

The reaction equation of charge exchange is:

$$D^0 + A^Z \rightarrow D^+ + (A^{Z-1})^*, \quad (1)$$

where a beam deuterium atom D^0 transfers an electron to a fully stripped carbon ion of charge Z, producing a deuterium ion and a hydrogen-like carbon ion in an excited state. The de-excitation process (CVI, n = 8 - 7) of A^{Z-1} emits visible photons which can be analyzed in a spectroscopic method. Actually, the composite CVI spectrum observed by each line-of-sight (l.o.s) mainly consists of three components, i.e., the active, passive and edge spectrum [12]. The active component should be extracted analytically. The calculation procedure for the carbon ion density is summarized as follows: a) the neutral beam density is first calculated with the beam attenuation process. b) The relative population between the ground state H(1 s) and excited state H^*(n = 2) of the beam atoms (namely the beam population) is then calculated, which participates in the charge exchange with the naked carbon ion. c) Finally the carbon ion density is derived from the absolutely calibrated active CVI (n = 8 - 7, 529.1 nm) intensity. The relevant atomic processes such as beam stopping, beam population and charge exchange emission are sketched in Fig. 2, with their reaction rates available in the open-ADAS data base which are calculated with the collisional–radiative models [13].

In general, impurity nuclei presented in the plasma are involved in the calculation of the effective reaction rates such as beam stopping and beam population. Therefore, the effect of mixed impurity plasma needs to be considered. The hydrogen nuclei are often the most important for the reaction coefficients since the fractional impurity concentrations are small. From this point of view, the impurity densities can only be derived in a self-consistent iterative loop. Because of the collision energy dependence of the cross-sections, the beam attenuation procedure, beam populations and charge exchange emission rates are determined respectively for the full (E_b), one-half (E_b/2) and one-third (E_b/3) fractional beam energy components in this work.

The radial profiles of plasma parameters at 645 ms in Shot 31572 used for the carbon ion density calculation are shown in Fig. 3. In Fig. 3 (a), the profiles of ion temperature and toroidal plasma rotation velocity are measured by the CXRS diagnostic employed in this work, and Fig. 3 (b) shows the Abel-inverted electron density profile measured by the FIR interferometer [14] and the electron temperature profile by the ECE diagnostic [15].

3.1 Calculation of beam attenuation process

A numerical calculation of the beam attenuation factor $\zeta_E = n_{\mathrm{beam}}(\rho)/n_{\mathrm{beam}}(\rho = 1)$ for each beam energy component, integrating the local effective beam stopping cross-section in terms of electron density n_e along the beam path from plasma boundary to one normalized radius ρ, is expressed as

$$\zeta_E = \exp\left\{-\int_1^{\rho} n_e(\rho)\cdot\left(\sum_{i=1} Z_i\cdot c_i(\rho)\cdot\sigma^{\mathrm{eff}}_{\mathrm{stop},i}(E)\right)dl\right\}, \quad (2)$$

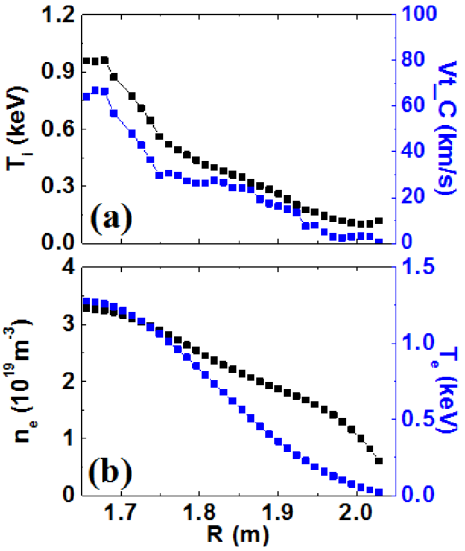

Fig. 3 Radial profiles of plasma parameters (a) T_i and V_t, and (b) n_e and T_e at 645 ms in Shot 31572.

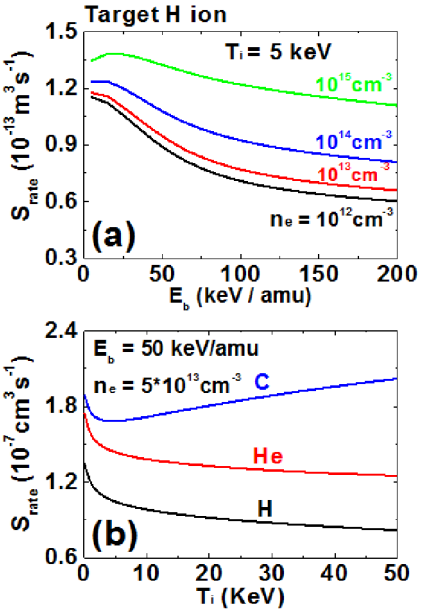

Fig. 4 Dependence of the beam stopping rates on (a) collisional beam energy under different electron densities and (b) ion temperature for different target ion species.

where $\sigma^{\text{eff}}_{\text{stop},i}$ denotes the local effective beam stopping cross-section for a specific nucleus with charge Z, and c_i is its local ion concentration. Obviously, the beam stopping is a total effect of the impurity-mixed plasma, and here an electrical neutrality assumption is applied. The beam stopping cross-section includes ionizations by the electron and ion collision (the latter being more efficient), as well as the charge transfer loss. The effective beam stopping rate S_{rate}, defined by $\sigma^{\text{eff}}_{\text{stop},i} \cdot v_b$ with v_b the collision velocity between the beam particle and target ion, is a function of plasma parameters such as ion temperature, electron density and beam atom collision energy, as shown in Fig. 4. The data

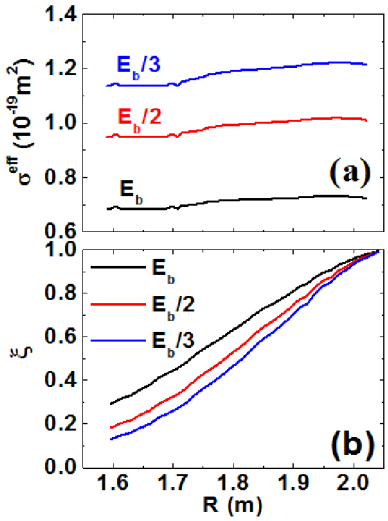

Fig. 5 (a) Beam stopping cross-section and (b) attenuation factor for each beam energy component along the beam path. Components: E_b, black; $E_b/2$, red; $E_b/3$, blue, as represented in the following figures.

are from the rapid-look-up tables in ADAS data format of ADF21. Obviously, it is more sensitive to the beam atom impact energy and the electron density, as shown in Fig. 4 (a), while it is less sensitive to the ion temperature. Moreover, the beam stopping rates in pure H-, He- and C-plasmas are compared, and it increases with the charge of the fully ionized target ion, as shown in Fig. 4 (b).

Seen from Eq. (2) an initial impurity concentration estimate is needed. For example, the flat concentration profiles of He^{2+} of 2%, C^{6+} 1.8%, and O^{8+} 0.5% are assumed. As a result, the beam stopping cross-sections along the beam path can be calculated for the three beam energy components, as shown in Fig. 5 (a). In the following, the beam attenuation factor ζ is calculated, as shown in Fig. 5 (b).

3.2 Calculation of neutral beam density

The aim of the beam attenuation calculation is to derive the neutral beam density. For the beams extracted from the four ion sources, they converge with horizontal and vertical focal length of 4.33 m and 5.33 m respectively, along the injection axis. Actually, the beam profile is non-circular transverse to the beam axis and herein is simplified by a Gaussian shape on the horizontal plane. The beam is presumed to be propagated from a point-like ion source on the horizontal plane with an equivalent distance of 3.5 m from the single point to the plasma center. This equivalent distance, accompanied by a beam divergence angle of 44 mrad determining the beam e^{-1} radius, is deduced by the aid of a beam trace program. The line integrated beam density for each beam energy component along the line-of-sight (l.o.s) across the neutral beam profile can be expressed as

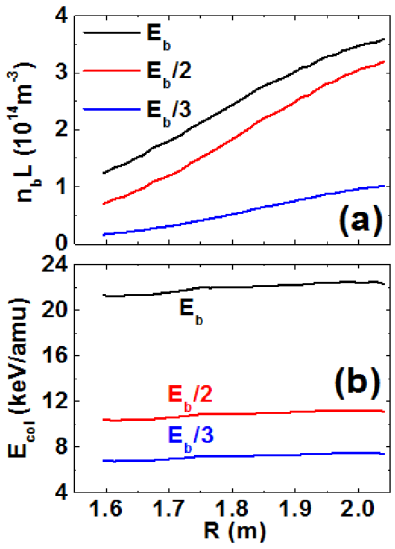

Fig. 6 (a) line integrated beam densities and (b) beam collision energies modified by the toroidal plasma rotation for the three beam energy components.

$$\int n_b ds = \frac{P \cdot f \cdot \zeta / \sin\theta}{e \cdot E \cdot v \cdot \sqrt{\pi} \cdot w_\perp}, \tag{3}$$

where P is the total NBI power in unit of W, f is the power proportion of each beam energy component, E is the beam atom energy in keV/amu, v is the beam velocity in m/s, θ is the angle between the l.o.s and the beam axis, and $w_\perp$ is the horizontal beam e^{-1} radius (beam half-width at 1/e height) [16].

One of the methods for determining the beam components is the Doppler shift of D_α Balmer lines. By introducing an effective cross-section (σ_{BES}) for Doppler-shifted D_α emission for a deuterium ion beam, the fraction of D^+, D_2^+ and D_3^+ ion beam entering the plasma boundary can be obtained as follows:

$$\zeta_1 : \zeta_2 : \zeta_3 = \frac{I_1}{\sigma_{BES}^{(1)}} : \frac{I_2}{\sigma_{BES}^{(2)}} : \frac{I_3}{\sigma_{BES}^{(3)}}, \tag{4}$$

where I_i (i = 1, 2 and 3) stand for the emissivity measured by an outmost channel (R = 2.04 m) of a BES diagnostic in parallel. In this case, the power proportion for the full (E_b), one-half ($E_b/2$) and one-third ($E_b/3$) fractional beam energy components are 0.73, 0.23 and 0.04 respectively. The net neutral beam input power is determined by the empirical scaling laws in HL-2A tokamak [11], and the NBI power is 630 kW in Shot 31572. As a result, the line integrated beam densities for each beam energy component are calculated and shown in Fig. 6 (a).

Note that the collision energy between the beam atom and plasma ion is not a constant along the beam trajectory, and it is corrected by the toroidal plasma rotation, as shown in Fig. 6 (b). The rotation-modified beam energy E_{col} can be expressed as follows:

$$E_{col} = E_b + \frac{1}{2} m \cdot v_t^2 - m \cdot \vec{v}_b \cdot \vec{v}_t, \tag{5}$$

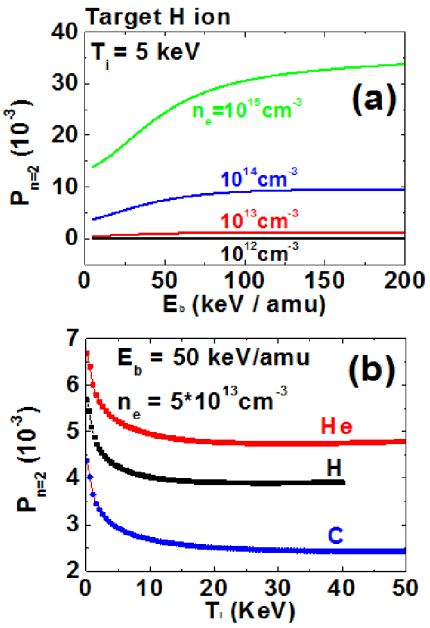

Fig. 7 The beam population as functions of (a) collisional beam energy under different electron densities and (b) ion temperature for different target ion species.

where E_b is the beam particle energy, m is the deuterium atom/ion mass, $\vec{v}_b$ is the beam atom velocity, and $\vec{v}_t$ is the local toroidal rotation velocity.

3.3 Calculation of beam population and charge exchange emission rates

Both the ground-state and excited state deuterium atoms contribute to the change-exchange excitation of impurities [17]. The excited deuterium-atom fractions, i.e., relative population of $H^*(n = 2)$ to H(1 s) in unit beam atom donor, are evaluated. The dependences of this population on the beam atom collision energy, electron density and ion temperature are extracted from the ADF22 data format, as shown in Fig. 7. The beam population probability in a plasma with different impurity concentrations can be calculated by the following relation:

$$P_{n=2}^{\text{eff}} = \sum_{i=1} Z_i \cdot C_i(\rho) \cdot P_{n=2}^i(\rho),$$

where $P_{n=2}^i(\rho)$ is the beam population probability in pure ion species plasmas, as applied for the beam stopping rates. The beam population for each energy component along the beam path is shown in Fig. 8 (a). Obviously, the excited components increase from the plasma edge to core, and they amount to only about 0.2% for the n = 2 level.

The effective charge exchange emission rates for C^{6+} ions are calculated with the H(1 s) and $H^*(n = 2)$ atom donors respectively for each beam energy component. This rate, obtained from the ADF12, is dependent on the beam atom impact energy, electron density, ion temperature and Z_{eff}. The cross-sections for transfer from excited atoms are much larger than those from the ground state, i.e., the re-

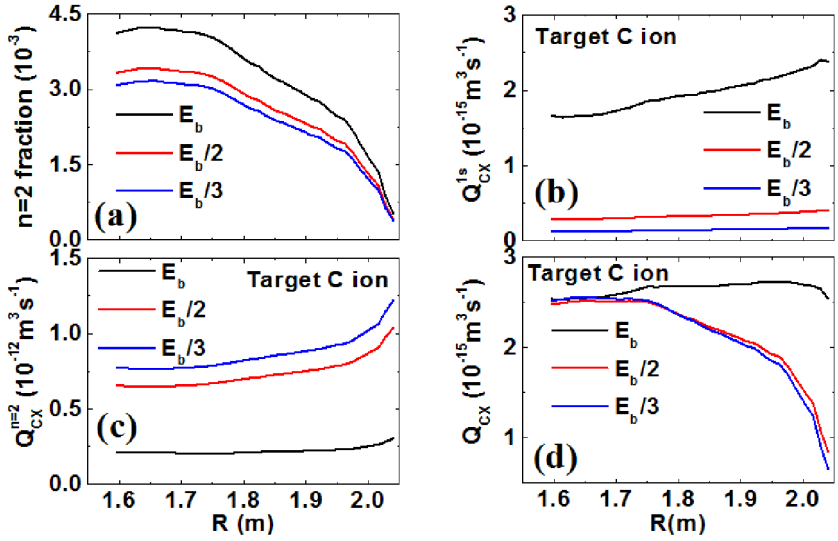

Fig. 8 (a) Beam population of $H^*(n=2)$ to H(1 s) for each beam energy component along the beam trajectory. The effective charge exchange emission rates for C^{6+} with incident H(1 s) and $H^*(n=2)$ are shown in (b) and (c) respectively. (d) Total charge exchange emission rates calculated by Eq. (6).

action rates with $H^*(n=2)$ donor are three orders of magnitude larger than that with the H(1 s) donor, as compared in Fig. 8 (b) and (c). Also seen from Fig. 8 (c), the excited beam atoms exchange charge more efficiently for the $E_b/3$ and $E_b/2$ components than for the full-energy component. Thus, when the beam current in the low-energy components is comparable to that in the full-energy component, excited atoms cannot be disregarded if their concentrations are of the order of 1%. Taking the excited component in Fig. 8 (a) into account, the total charge exchange emission rate for each beam energy component is given by

$$Q_{CX}^{E} = P_{n=2} \cdot Q_{CX}^{n=2} + (1 - P_{n=2}) \cdot Q_{CX}^{1s}, \tag{6}$$

as shown in Fig. 8 (d). Clearly, the contribution of excited states to the effective charge exchange emission rates becomes comparable to the contribution from the ground state in the plasma core region for the full-energy beam component. Here the contribution of deuterium in the n = 3 level and above to the charge-transfer cross-section is not considered. Nevertheless, their contribution is nearly one order of magnitude smaller than that from the n = 2 state [17].

3.4 Calculation of the carbon ion concentration profile

The active CVI (529.1 nm) photon flux Φ_{CVI} measured by the toroidal CXRS diagnostic is determined as follows:

$$\Phi_{CVI} = \frac{1}{4\pi} n_Z(\rho) \cdot \sum_k Q_{CX}^{E_k} \cdot N_{b,k}, \tag{7}$$

where $n_Z(\rho)$ is the local CVI ion density to be calculated, $Q_{CX}^{E_k}$ is the effective charge exchange emission rate for each beam energy component, and $N_{b,k}$ is the line integrated beam density in the kth energy component. The observed CX signal is contributed from the three beam energy fractions, and the extractive Φ_{CVI} is shown in Fig. 9 (a). Here the plasma parameters such as T_i, n_e and n_z are assumed to be constant along the intersection of viewing chord with the neutral beam because the l.o.s of CXRS diagnostic is nearly tangential to the magnetic flux surface at the intersection. Consequently, the calculated profiles of carbon ion density from Eq. (7) and concentration are shown in Figs. 9 (b) and (c) respectively. Here, a convergent iterative process is necessary to derive the carbon ion density profiles. For the profile of carbon ion concentration, it is nearly flat at $\rho > 0.5$ region and the concentration is ~4%, while it embodies an impurity accumulation at plasma core. Consequently, the local Z_{eff} indicated by the black squares in Fig. 9 (d) is calculated by

$$Z_{\text{eff}} = 1.0 + \sum_{\text{imp}} f_{\text{imp}} Z_{\text{imp}} (Z_{\text{imp}} - 1), \tag{8}$$

where f_{imp} is the impurity concentration for each species, and Z_{imp} is the ion charge. It is worth pointing out that the concentration profiles of impurity species are assumed to be flat except for the carbon ion. This assumption makes a rather small effect on the calculation of carbon ion concentration, since the fractional impurity concentrations are small and their changes have little influence on the effective reaction rates. Also, Z_{eff} measured by the visible bremsstrahlung is shown with a slightly hollow profile, indicated by the green triangles in Fig. 9 (d). Obviously, a difference of ~0.5 appears at plasma core.

In fact, the halo effect has not been involved for the carbon ion density calculation. The halo, a cloud of neutral atoms produced around the neutral beam, acts as an additional source for charge exchange processes with impuri-

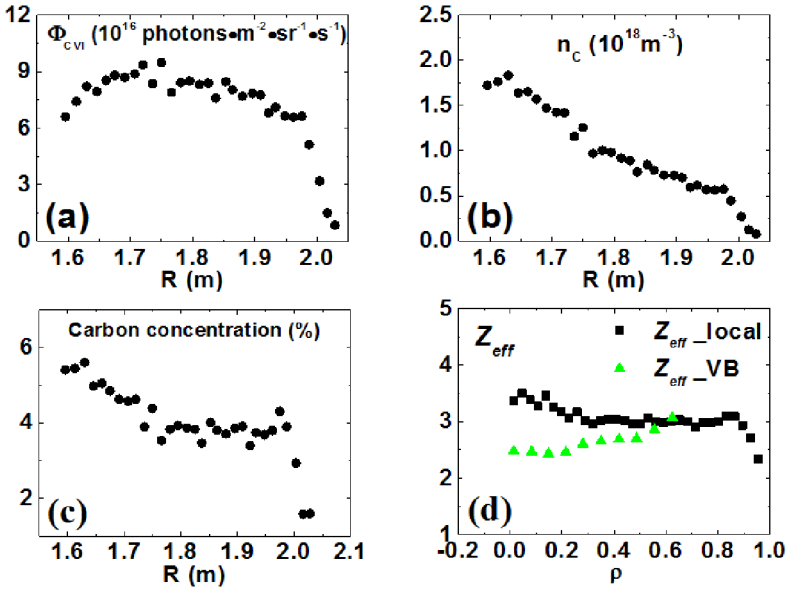

Fig. 9 (a) CVI (529.1 nm) flux profile measured by the toroidal CXRS diagnostic, (b) and (c) carbon ion density and concentration profiles respectively, and (d) $Z_{\rm eff}$ profiles calculated from local impurity concentrations (black squares) and visible bremsstrahlung (green triangles) respectively.

ties and contributes to the total active CVI photon flux [18]. Therefore, the carbon ion concentration in Fig. 9 (c), and thus the local $Z_{\rm eff}$ profile indicated by the black squares in Fig. 9 (d) are overestimated. Also, the beam geometry such as ion source location and beam divergence angle is an error source of carbon ion density calculation.

4. Conclusion and Discussion

The absolute carbon impurity density profiles are obtained based on the neutral beam density calculated with a beam attenuation process on HL-2A tokamak. The neutral beam densities, beam populations and charge exchange emission rates are determined respectively for the full (E_b), one-half (E_b/2) and one-third (E_b/3) fractional beam energy components. The naked carbon ion concentration is $\sim 4\%$ in the timeslice of 645 ms in Shot 31572.

Since the beam attenuation factor in Eq. (2) suffers an increasing error along the beam path due to the uncertainties in the beam stopping cross-section, one alternative way is to combine the CXRS and BES intensity with the local beam density calculation omitted [5, 19]. Respect to this method, a tri-band and high spectral resolution spectrometer is newly developed on HL-2A tokamak, which is able to provide the measurements of He II (468.57 nm), C VI (529.1 nm) and Dα (656.1 nm accompanied by BES) simultaneously. Another advantage of this method is that the beam geometries such as ion source location and beam divergence angle are not involved. The data processing is under development, and the impurity density calculated by the two methods will be compared. Nevertheless, the influence of halo neutrals on the impurity density determination will be estimated in our future work for both of the two methods.

Acknowledgements

The authors would like to thank the HL-2A team for their help in the experiments. This work is supported in part by the Sichuan Science and Technology Program under Grant No. 2020JDRC0125, the National Key Research and Development Program of China under Grant Nos. 2017YFE0301306 and 2017YFE0301106, and the Nature Science Foundation of China under Grant Nos. 11675050, 11875020, 11847071 and 11320101005.

[1] R.J. Fonck and R.A. Hulse, Phys. Rev. Lett. **52**, 530 (1984).
[2] E.J. Synakowski *et al.*, Phys. Rev. Lett. **65**, 2255 (1990).
[3] K. Ida *et al.*, Phys. Rev. Lett. **58**, 116 (1987).
[4] O. Marchuk *et al.*, Rev. Sci. Instrum. **79**, 10F532 (2008).
[5] A. Boileau *et al.*, Plasma Phys. Control. Fusion **31**, 779 (1989).
[6] A. Kappatou *et al.*, Rev. Sci. Instrum. **83**, 10D519 (2012).
[7] Z.Y. Cui *et al.*, Nucl. Fusion **55**, 093034 (2015).
[8] L. Liu *et al.*, Fusion Eng. Des. **143**, 41 (2019).
[9] Z.Y. Cui *et al.*, Nucl. Fusion **53**, 093001 (2013).
[10] Y.L. Wei *et al.*, Rev. Sci. Instrum. **85**, 103503 (2014).
[11] J.Y. Cao *et al.*, Chin. Phys. Lett. **32**, 052902 (2015).
[12] M.G. von Hellermann *et al.*, Physica Scripta **T120**, 19 (2005).
[13] https://open.adas.ac.uk/
[14] Y.G. Li *et al.*, Rev. Sci. Instrum. **88**, 083508 (2017).
[15] Z.B. Shi *et al.*, Rev. Sci. Instrum. **85**, 023510 (2014).
[16] M.G. von Hellermann *et al.*, Atoms **7**, 30 (2019).
[17] R.C. Isler and R.E. Olson, Phys. Rev. A **37**, 3399 (1988).
[18] E. Busche *et al.*, Plasma Phys. Control. Fusion **39**, 1327 (1997).
[19] R.J.E. Jaspers *et al.*, Rev. Sci. Instrum. **79**, 10F526 (2008).